SLICING THE MONOCEROS OVERDENSITY WITH SUPRIME-CAM

Blair C. Conn[1], Noelia E. D. Noël[1,2], Hans-Walter Rix[1], Richard R. Lane[3], Geraint F. Lewis[4],
Mike J. Irwin[5], Nicolas F. Martin[1,6], Rodrigo A. Ibata[6], Andrew Dolphin[7], and Scott Chapman[5]

[1] Max Planck Institut für Astronomie, Königstuhl 17, 69117 Heidelberg, Germany
[2] ETH Zürich, Institute for Astronomy, Wolfgang-Pauli-Strasse 27, Building HIT, Floor J, CH-8093 Zurich, Switzerland
[3] Departamento de Astronomía, Universidad de Concepción, Casilla 160-C, Concepción, Chile
[4] Sydney Institute for Astronomy, School of Physics, The University of Sydney, A28, Sydney 2006, Australia
[5] Institute of Astronomy, Madingley Road, Cambridge CB3 0HA, UK
[6] Observatoire de Strasbourg, 11 Rue de l'Université, F-67000 Strasbourg, France
[7] Raytheon Company, P.O. Box 11337, Tucson, AZ 85734-1337, USA

ABSTRACT

We derive distance, density, and metallicity distribution of the stellar Monoceros Overdensity (MO) in the outer Milky Way, based on deep imaging with the Subaru Telescope. We applied color–magnitude diagram fitting techniques in three stripes at galactic longitudes, $l \sim 130°$, $150°$, $170°$, and galactic latitudes, $+15° \leqslant b \leqslant +25°$. The MO appears as a wall of stars at a heliocentric distance of $\sim 10.1 \pm 0.5$ kpc across the observed longitude range with no distance change. The MO stars are more metal-rich ([Fe/H] ~ -1.0) than the nearby stars at the same latitude. These data are used to test three different models for the origin of the MO: a perturbed disk model, which predicts a significant drop in density adjacent to the MO that is not seen; a basic flared disk model, which can give a good match to the density profile but the MO metallicity implies the disk is too metal-rich to source the MO stars; and a tidal stream model, which, from the literature, brackets the distances and densities we derive for the MO, suggesting that a model can be found that would fully fit the MO data. Further data and modeling will be required to confirm or rule out the MO feature as a stream or as a flaring of the disk.

Key words: Galaxy: disk – Galaxy: structure

Online-only material: color figures, Supplemental data (FITS) file (tar.gz)

1. INTRODUCTION

The Monoceros Overdensity (MO) is an extensive stellar structure found in the outer regions of the Milky Way at Galactocentric distances of ~ 15–18 kpc. It was originally discovered in the Sloan Digital Sky Survey (SDSS) by Newberg et al. (2002) and subsequent observations reveal a similar structure in many directions around the Galaxy (Yanny et al. 2003; Ibata et al. 2003; Crane et al. 2003; Conn et al. 2005a, 2005b, 2007, 2008; Martin et al. 2006; Casetti-Dinescu et al. 2008; Sollima et al. 2011). From this, it has been concluded that it forms a coherent structure from Galactic longitudes of $l = 60°$–$300°$ and straddles both sides of the Galactic plane. While the approximate extent of the MO is tentatively mapped, its origins are somewhat obscure.

The MO formation scenarios fall into three broad categories: tidal tails from an accreting dwarf galaxy (Martin et al. 2004; Peñarrubia et al. 2005; Michel-Dansac et al. 2011); misidentification of normal Galactic warp/flare profiles (Momany et al. 2004, 2006; Moitinho et al. 2006; López-Corredoira et al. 2007; Hammersley & López-Corredoira 2011); and perturbed disk scenarios whereby a close encounter with a massive satellite induces rings in the outer disk from local material (Kazantzidis et al. 2008; Gómez et al. 2012; Purcell et al. 2011).

If we consider each scenario briefly then the first scenario is a Galactic accretion event, where the MO is envisioned to be the tidal tails of a dwarf galaxy merging in-plane with the disk. Such a scenario is attractive since it links with the Λ-cold-dark-matter cosmology where galaxies form via successive accretion events (White & Rees 1978) and the discovery of many stellar streams in the halo of the Milky Way (Newberg et al. 2002; Belokurov et al. 2006; Grillmair 2006, 2009). The proposed progenitor for the MO is the putative Canis Major dwarf galaxy,

first discussed in Martin et al. (2004). If true, the MO could be a relic of formation as discussed in Freeman & Bland-Hawthorn (2002).

The second scenario is used to explain both the stellar overdensity in Canis Major and the MO in terms of standard properties of a galactic disk, that is, the warp and the flare. The Milky Way disk is observed, with various tracers, to warp up in the first two quadrants and warp down in the second two quadrants. For instance, López-Corredoira et al. (2002) follow this feature with red clump giant stars while Yusifov (2004) uses pulsars as tracers. As the density of the disk drops with increasing galactic radii, it thickens and flares. The Canis Major dwarf galaxy is therefore the disk of the Galaxy dipping below the plane and the MO is the intersection of the flaring disk at high latitudes above the plane.

Finally, the third scenario invokes the interaction between a dark matter satellite and disk to induce the formation of rings at large galactic radii. The repeated passage of these satellites through the disk drives the formation of spiral arms and rings. This has been tested for low inclination satellite encounters (Kazantzidis et al. 2008) and more recently for the Sagittarius dwarf galaxy (Gómez et al. 2012; Purcell et al. 2011), which is on a polar orbit.

All of these scenarios are able, with varying levels of success, to fit the general spatial and kinematic profiles of the MO and previous attempts to find some decisive evidence or prediction has not ruled out any of these possibilities. More and more observations of the MO, both photometric and spectroscopic are becoming available (SEGUE,[8] PanSTARRS,[9] SkyMapper, etc.) and so these degeneracies may be broken soon.

---

[8] Sloan Extension for Galactic Understanding and Exploration.
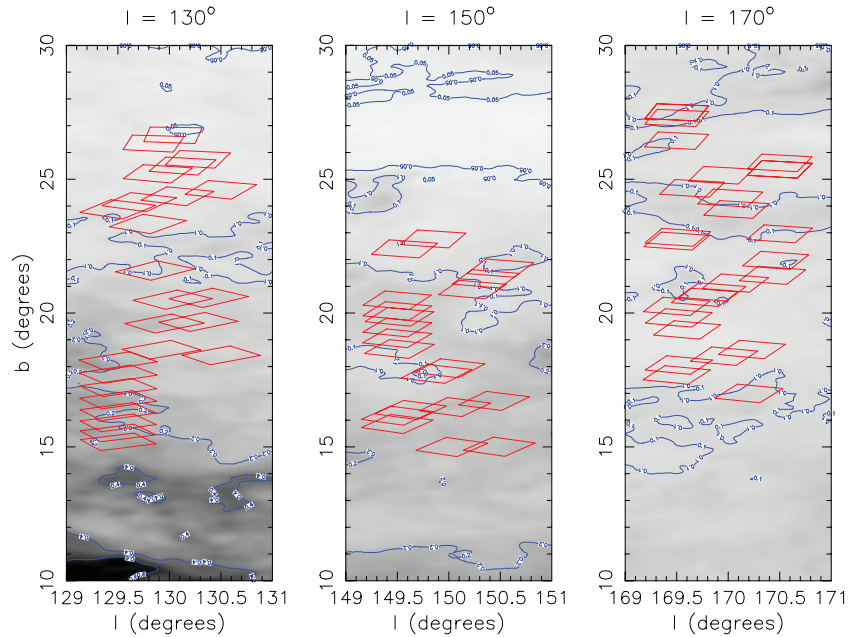[9] Panoramic Survey Telescope and Rapid Response System.

Figure 1. Survey layout against Galactic extinction from the dust maps from Schlegel et al. (1998). The red polygons represent the position of the fields surveyed here. The final survey locations are the result of observational constraints and data quality issues. The gray scale shows the underlying dust extinction with the blue contours outlining the $E(B - V)$ values of 0.05, 0.1, 0.2, 0.4, and 0.6.

(A color version of this figure is available in the online journal.)

Table 1
Summary of Observations

Region	Fields	Date Observed	Filter	Median Seeing
130 stripe	1–16	2007 Nov 9	g, r	$0\rlap{.}''71, 0\rlap{.}''62$
. . .	20–32	2008 Jan 8	g	$0\rlap{.}''78$
. . .	17–29	2008 Jan 8	r	$0\rlap{.}''69$
150 stripe	1–32	2007 Nov 9	g	$0\rlap{.}''59$
. . .	1–32	2008 Jan 8	r	$0\rlap{.}''74$
170 stripe	1–32	2007 Nov 9	g, r	$0\rlap{.}''47, 0\rlap{.}''5$

In order to shed light into the above dilemma, we secured observations using the Subaru Telescope. Our goal is to investigate the spatial density profile of the MO and also to compare our observational results with the different theoretical scenarios presented in the literature. In Section 2 we discuss the data preparation in terms of the observations, reduction, and calibration of the data set. Section 3 outlines the analysis of the color–magnitude diagrams using CMD-fitting techniques. In Section 4 we compare our findings with the current scenarios of formation for the MO and in Section 5 we present our conclusions.

2. DATA PREPARATION

2.1. Observations and Reduction

The data were collected using the SUPRIME-CAM Wide Field Imager on the Subaru Telescope in Hawaii. SUPRIME-CAM is a 10 chip camera with a field of view of $34' \times 27'$ and a pixel scale of $0\rlap{.}''20$. These observations took place in Service mode and were carried out on 2007 November 9 and 2008 January 1. These observations are summarized in Table 1. Roughly 180 frames were taken in two filters, Sloan g and r, and arranged into the three stripes across the thick disk of the Galaxy. Each g frame was 124 s and each r frame was 76 s. Figure 1 shows the survey layout for each stripe with the location of the fields depicted as red polygons overplotted on the local dust extinction contours. Implementing the program in this manner with SUPRIME-CAM allows for deep observations to be obtained across large areas in a short period of time as required by this study. The final survey locations are the result of observational constraints and data quality issues.

The data were reduced using the Cambridge Astronomical Survey Unit Wide Field Camera Pipeline (Irwin & Lewis 2001). This pipeline was originally developed for the Isaac Newton Telescope Wide Field Camera and has since been modified to work on most of the Wide Field Imagers available today. The pipeline reduced data have been bias-subtracted, flat-fielded using twilight sky flats and then flat-fielded again using a dark sky super-flat. Following this, the photometry and astrometry have been determined using the same pipeline. The accuracy and completeness of the photometry will be discussed in Section 2.4. The astrometry, based on the Two-Micron All-Sky Survey (2MASS) point source catalog, is typically accurate to between 0.2 and 0.3 arcsec.

2.2. Correcting the Photometry Using SDSS

Having generated the catalog of sources and classifying them, the photometric calibration was performed by cross-matching sources with the SDSS Data Release 6 (Adelman-McCarthy et al. 2008). At the time of the survey only a few of the fields overlapped with the SDSS and so the calibration was performed on those fields and then applied to the others according to their date of observation. Two offsets were needed as it was noticed that Chip 10 has a much lower efficiency than the rest of the array. Since the 150 stripe also had SDSS corrections available, when correcting the other fields the choice between these two was based on which night those observations were taken on. The final photometric solution has a typical scatter of 3.5% in the g band and 2.4% in the r band around the SDSS values.
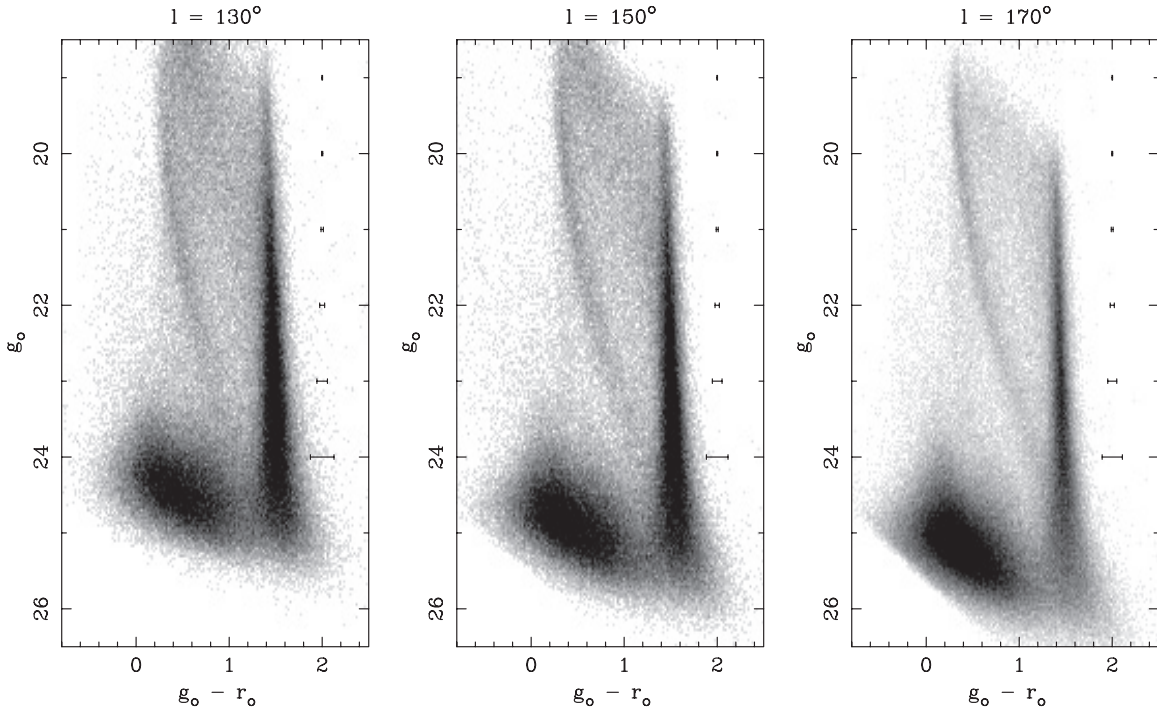
Figure 2. Deep Hess CMDs of point sources obtained for each of the three stripes. The data have been extinction corrected according to Schlegel et al. (1998) and Bonifacio et al. (2000). The cloud of sources in the bottom left of each panel stems from unresolved galaxies. A difference in the image quality between the observations of $l = 130°$ and the $l = 170°$ stripe is responsible for the increase in depth of the resulting CMDs (see Table 1). Main-sequence turnoff (MSTO) stars, which we associated with the MO, are found at $g_o - r_o \sim 0.4$, $g_o \sim 19.5$. The strong overdensity of stars at $g_o - r_o \sim 1.5$ are the local low mass dwarf stars.

Table 2
Mean Magnitude at the 50% Completeness Level (m_c) and Typical Width of the Rollover Function (λ) for Each Filter

Region	m_c ($g_\circ$)	m_c ($r_\circ$)	λ
130 stripe	24.2	23.2	0.73
150 stripe	24.8	23.8	0.55
170 stripe	25.0	24.2	0.70

Note. See Equation (1).

2.3. Correcting the Photometry Using Dust Extinction Maps

After the initial correction using SDSS, a correction based on the dust maps of Schlegel et al. (1998) combined with the adjustment of Bonifacio et al. (2000) was implemented. The final photometry is presented as Hess CMDs in Figure 2. In general, the dust contamination is less than an $E(B - V)$ of 0.2, for the majority of the survey. The data here have been extinction corrected and represent all the fields for each stripe combined into one figure.

2.4. Magnitude Completeness

For those fields which overlap with each other, the completeness of this sample has been determined in the same manner as used in the 2MASS All-Sky Point Source Catalogue (Skrutskie et al. 2006). By determining the fraction of stars that are detected in both overlapping images as a function of magnitude with respect to the total number of stars observed, an estimate of the completeness can be made. This photometric completeness curve is then fit by the Logistic function:
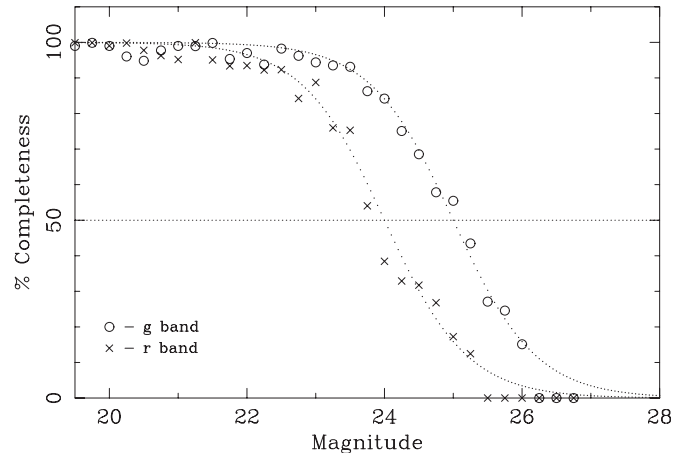
$$CF = \frac{1}{(1 + e^{(m-m_c)/\lambda})},$$ (1)

Figure 3. Example completeness data and fit for a field in the $l = 150°$ stripe using the stars in the pointings which overlap. The completeness is determined by whether a star detected in either frame is recovered in the other frame. This is then binned by magnitude and presented as the percentage completeness of recovered divided by detected. Circles for the g-band objects and crosses for the r-band objects.

where m is the magnitude of the star, m_c is the magnitude at 50% completeness, and λ characterizes the width of the rollover from 100% to 0% completeness. The average values found in each field are presented in Table 2 and an example completeness profile is shown in Figure 3.

2.5. Survey Field CMDs

The pipeline provides a set of classifications for different objects. We are interested in those classified as stellar and possibly stellar objects. The detailed information on the categories is given in Irwin & Lewis (2001). In short, each processed frame

in the pipeline is analyzed using an object detection algorithm based on Irwin (1985, 1997). Generated parameters include information on position, intensity, and shape. To discriminate between background galaxies and real objects, three flux estimates are made: integration of the flux above the specific age; the detection isophote for each image is expanded using an elliptical aperture to perform a curve-of-growth analysis; and a "poor man's" point spread function (PSF) fit using a radius equal to the FWHM. The stellar objects and possible stellar objects are then selected from all the fields within a given stripe and plotted in a single CMD. Figure 2 shows the three ($g_o - r_o$, g_o) deep Hess CMDs with each containing approximately 200,000 stars which correspond to the three longitudinal stripes of the survey. To allow the low density MO feature to be clearly visible, the CMD gray scale is scaled using the square root of the counts shown in each pixel. These exceptional CMDs, reaching more than 3 mag below the oldest MS turnoffs ($g_o \sim 19.5$), are the deepest observations of the MO to date. The CMDs show the old MS population along its complete extent from the blue turnoff region to faint red MS stars. The high quality of the photometry and the small errors on the main sequence allow us to secure the distance–metallicity degeneracy in the CMDs. This ensures we can quantitatively measure the stellar content of the MO.

3. DATA ANALYSIS

3.1. CMD-fitting Technique

In order to obtain the stellar populations' structure at the location of the MO we used the MATCH software package (Dolphin 2002) in its distance-fitting mode. MATCH was originally developed to obtain quantitative star formation histories and age–metallicity relations for systems in which all the stars are assumed to be at the same distance. For this purpose, the distance is fixed and the age and metallicity are independent variables. In this paper, we apply the CMD-fitting techniques to span the local stellar populations within the Milky Way. For this goal, we can no longer consider that all stars are equidistant and, thus, the distance is a free parameter. In order to limit the number of free parameters, we define a set of template stellar populations for comparison with the data.

In the same manner as explained in de Jong et al. (2010) we used the SDSS g and r isochrones provided by Girardi et al. (2004). Given that both the thick disk and stellar halo are known to have old stellar populations, we considered a fixed age range at ∼13 Gyr ($10.1 < \log[t/\mathrm{yr}] < 10.2$), 30% binary fraction, a Salpeter initial mass function (Salpeter 1955), and three metallicity bins, sufficient to describe the halo and thick disk: [Fe/H] $= -0.7$, [Fe/H] $= -1.3$, [Fe/H] $= -2.2$ (see de Jong et al. 2010 for more details). Stars with intermediate metallicities are inferred from the relative weight of these three template populations. The thin disk stars are avoided as they have a broader range of ages and metallicities which would make it difficult to disentangle from a combination of only three different metallicity templates. To avoid edge effects, the model templates were created for distance moduli between 7 (∼250 pc) and 22 (∼250 kpc) in steps of 0.2.

The basis of MATCH is the Hess diagram, a binned CMD in which the value of each bin is the square root of the number of stars. Synthetic Hess diagrams are then created for a range of ages and metallicities initially assuming 1 $M_\odot$ yr^{-1} star formation rate (SFR) which is then scaled and combined to best match the observed diagram. The synthetic diagrams are convolved with the photometric errors and completeness profile of the data to provide a realistic comparison with the data. When comparing the observed CMD with the synthetic CMD, MATCH uses a Poisson Maximum Likelihood statistic to determine the best-fitting single model or linear combination of models.

We used stars in the magnitude range $18.5 < g_o < 23.0$ and $18.0 < r_o < 23.0$ and in the color range $0.1 < g_o - r_o < 1.1$ (Figure 4). These color cuts ensure that we do not include faint, red stars belonging to the thin disk, while the magnitude cuts ensure that we do not include spurious objects such as misclassified galaxies. For each population template, MATCH provides the SFR in $M_\odot$ yr^{-1} for each distance modulus bin. The SFRs are then converted into stellar mass density.

Figure 4 shows an example of an observed CMD and its best-fit model CMD for a single frame in stripe $l = 130°$. For each single frame one Hess diagram is created. The observed CMD is shown on the left-hand side; the region used in our analysis is depicted with the dot-dashed rectangle. The four panels on the right-hand side are the observed Hess CMD (top left), the model Hess CMD (top right), the residual Hess CMD after subtracting the model from the data (bottom left), and the residual significance, based on the number of stars expected in the model Hess diagram (bottom right). The model CMD reproduces well the main features of the observed CMD, such as the main plume of old main-sequence turnoff (MSTO) stars, especially since we assumed only a simple model population.

3.2. Density and Metallicity Gradients

MATCH provides the SFR (in $M_\odot$ yr^{-1}) corresponding to each population template for each distance modulus bin and this is transformed into a stellar mass density. Figure 5 shows the density profiles for the lower half of the $l = 130°$ stripe plotted against heliocentric distance. A Sérsic profile is then fit to the underlying stellar population and is shown overplotted on the data. The stellar density shows a clear decrease with distance and includes a conspicuous deviation in the distance range $7 < d\,(\mathrm{kpc}) < 13$. This "excess" in the density distribution, present in all our fields, is due to the MO. The steep exponential profile in the inner ∼5 kpc is due to the contribution of the thick disk population. From ∼5 kpc onward the inner halo component dominates up to ∼20 kpc when the outer halo begins to rule, producing a flattening in the density profile. This corresponds well to the density profiles reported in de Jong et al. (2010).

The depth of the data allows us to unequivocally delineate the density of stars in the MO. In order to obtain a clear detection of the MO and to find out if there are differences with height above the plane, we gathered all the fields corresponding to each stripe into two halves: upper and lower latitudes, i.e., six halves in total, two per stripe. This improves the signal to noise of the MO as individual frames do not contain enough stars to perform the analysis. To quantify the resultant overdensities, we removed the smooth background stellar density distribution and fitted a Sérsic profile to the stellar mass density relation obtained from the CMD analysis. For each density profile, we took all the points within the 3σ values of the Sérsic fit and recalculated the density, thus removing the bulk Milky Way components from the distribution. The best-fit Sérsic parameters can be found in Table 3. The resultant residual for each of the six fields is shown in Figure 6. The upper panels represent the residuals of the total mass density in the upper latitude set and the lower panels are the same for the lower latitude set. All of the residuals show a bump at the location of the MO. The number density is relatively constant across the stripes for each latitude range, however, the
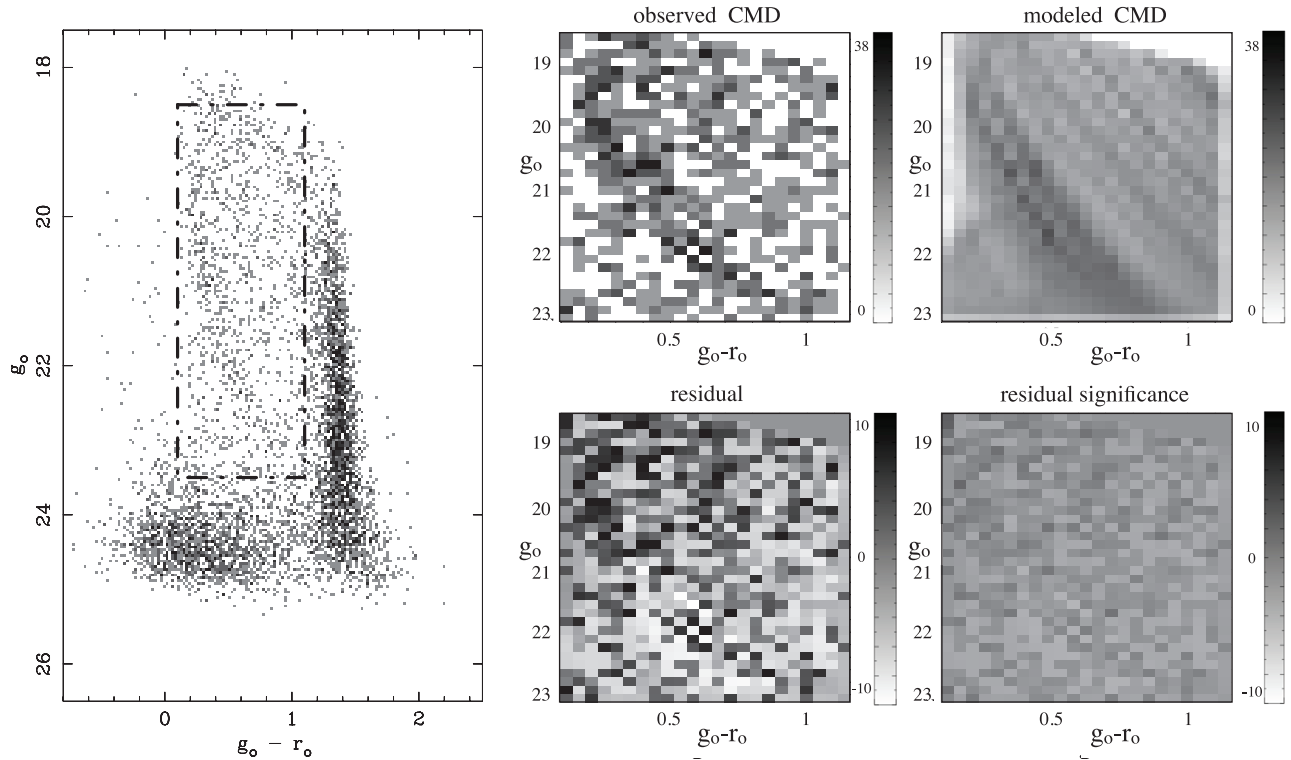
Figure 4. Left: an observed CMD for a single frame of the stripe $l = 130°$. The long dashed rectangle represents the region used in our analysis. The four panels to the right show the output of the CMD-fitting routine MATCH (see Section 3.1). The upper panels show the observed CMD (left) and best-fit model to the observed CMD (right). The lower panels are residuals after subtracting the model from the observed CMD (left) and residual significance (right) based on a fit parameter including the number of stars in the observed and model CMD. The gray scale bar represents the number of stars in the Hess diagram bins. The analysis was made in the regions $18.5 < g_o < 23.0$, $18.0 < r_o < 23.0$, and $0.1 < g_o - r_o < 1.1$ of the CMDs shown in Figure 2. In this way, we avoid the clump at $g_o > 23.0$ and $g_o - r_o < 1.0$ mainly due to unresolved background galaxies and local dwarf stars located at $(g_o - r_o) > 1.5$. As seen in Figure 3 we have 95% completeness at $g_o = 23.0$ and 90% at $r_o = 23.0$.
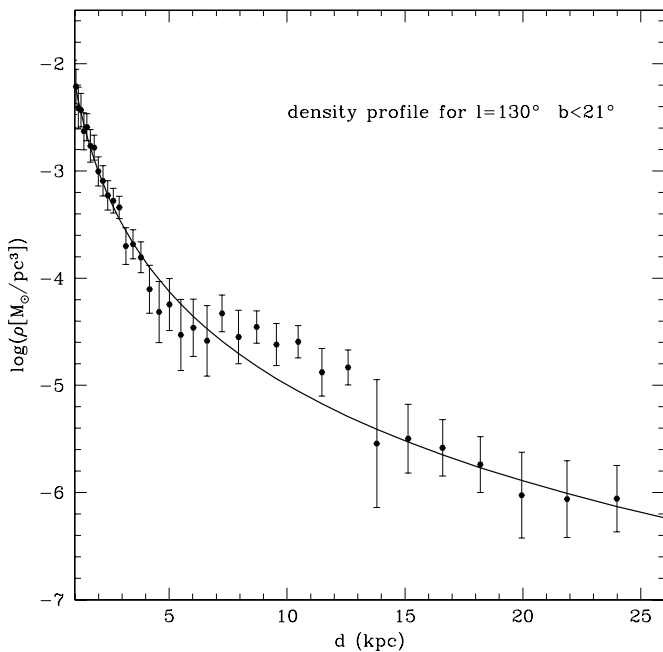

Figure 5. Mean stellar mass density distribution for the stripe with $l = 130°$, $b < 21°$. The stellar density decreases with increasing distance with a conspicuous deviation at around 10 kpc from the Sun, corresponding to the location of the MO. A Sérsic profile is fitted to the density distribution to remove the Milky Way background and allow for a cleaner detection of the MO. Error bars were calculated from the uncertainty associated with the density of each bin from the Monte Carlo tests. This is achieved by multiply resampling the stars within CMD space and re-running MATCH on each resampled population.

lower latitudes are consistently denser than the higher latitudes. Figure 6 also shows the location of the MO, denoted by D, which was found by fitting a Gaussian profile to the residual density peaks. The line-of-sight depth of the MO represents the FWHM of the best-fit Gaussian. The stellar number density of each of the six regions can also be found in Table 3, as well as the mean latitude, heliocentric distance, and line-of-sight depth.

Given the similarities between each of the stripes, we gathered all the stripes together to obtain metallicity profile. The total mass-weighted mean metallicity profile is shown in Figure 7. Although the smooth underlying Milky Way population has not been subtracted, the MO is still clearly visible. The metallicity distribution is at slightly higher distances than seen in the density profiles and deviates from the smooth background between 9 and 14 kpc heliocentric. It reaches a peak metallicity of $[Fe/H] \sim -1.0$ which is consistent with the photometallicities of the MO as determined through SDSS photometry by Ivezić et al. (2008).

4. DISCUSSION

These deep CMDs of the MO at three different galactic longitudes ($l = 130°$, $150°$, and $170°$) and covering a range of galactic latitudes ($+15° \leqslant b \leqslant +25°$) allow us to accurately constrain the structural properties of the MO in these directions. Figures 2, 5, and 6 show that the MO is easily identifiable at all stages of the analysis: it appears as a strong main-sequence-type feature in the CMDs; it shows a clear excess above the Sérsic fit to the bulk Milky Way components in the stellar density profiles; it occupies a distinct distance range within the sensitivity limits
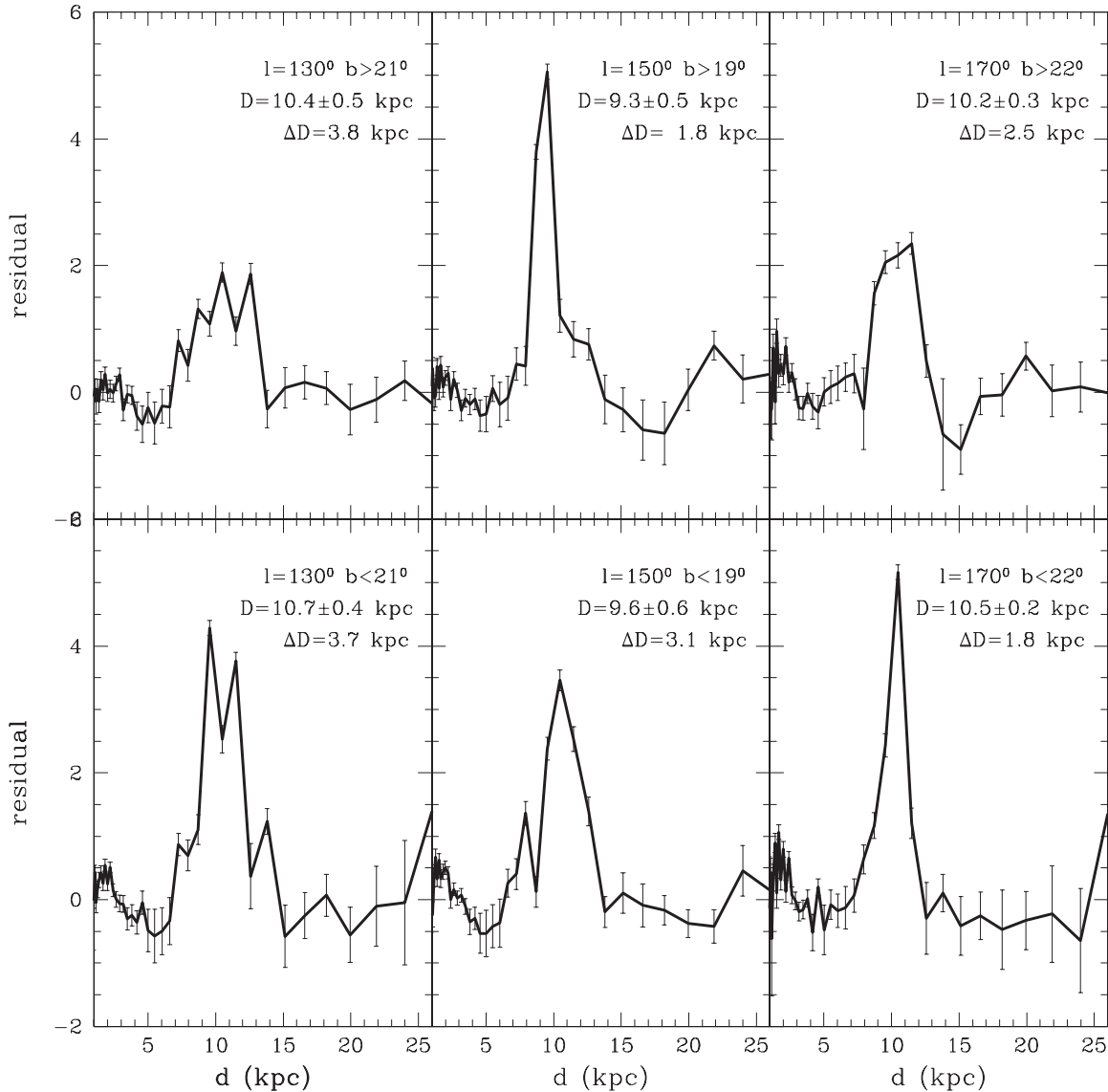
Figure 6. Residual density of the stream after subtracting a Sérsic profile fit, in the distance range of 1–25 kpc, to the smooth Milky Way component. The top panels are the residuals from the higher latitude half of each stripe, while the bottom panels are the residuals from the lower latitude half of the stripes. See Table 3 for the values obtained from this analysis. The distance to each MO detection is determined through a Gaussian fit to the residuals. The width of the MO is the FWHM of that Gaussian fit. This is shown as "D" and "ΔD" in each sub panel. The error on the distance is related to the error on fitting the Gaussian to the residual density profile.

Table 3
Results from the MATCH Analysis, Distance, Depth, and Density

Region	Mean Latitude ($b°$)	Distance Heliocentric (kpc)	Depth of MO (kpc)	Stellar Number Density (counts)	Sérsic Index/ Reduced χ^2	Sérsic Scale Length (kpc)
130 stripe (upper)	24	10.4 ± 0.5	3.8 ± 0.4	463	7.0/1.4	0.2
130 stripe (lower)	18	10.7 ± 0.4	3.7 ± 0.4	671	8.0/1.2	0.1
150 stripe (upper)	21	9.3 ± 0.5	1.8 ± 0.2	553	13.0/1.2	0.11
150 stripe (lower)	17	9.6 ± 0.2	3.1 ± 0.4	609	6.0/1.5	0.54
170 stripe (upper)	25	10.2 ± 0.3	2.5 ± 0.3	427	5.15/1.5	2.43
170 stripe (lower)	20	10.5 ± 0.2	1.8 ± 0.2	588	3.55/1.6	0.47

of the method; and it has a metallicity that strongly differs from the background Milky Way population. Figure 8 shows the locations of the MO with respect the Galactic center and the Sun. A line has been drawn at the Galactic radius of 17.0 kpc for reference. Each detection is shown illustrating its distance uncertainty and the width of the feature. In Sections 4.1–4.3, we will discuss the various formation scenarios in light of the

density profiles uncovered here. In Section 4.4, we will discuss the implications of the metallicity finding and its relevance to the outer disk.

4.1. The Monoceros Overdensity as a Tidal Stream

We compare our results with the only two current numerical simulations of Martin et al. (2004) and Peñarrubia et al. (2005).
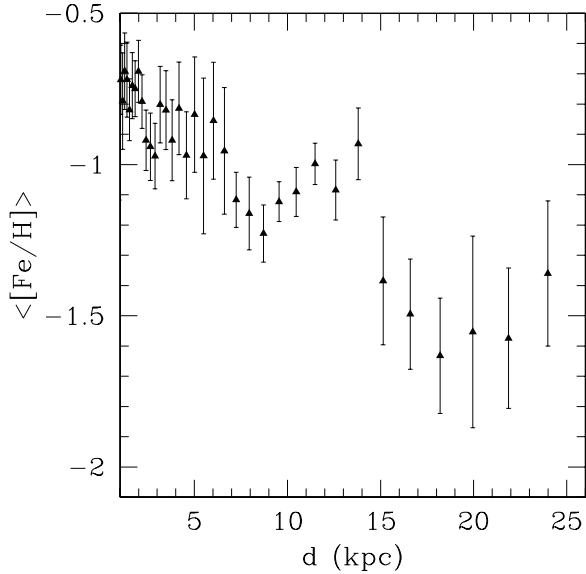
Figure 7. Mass-weighted mean metallicity from the MATCH fits, averaged over all latitudes and longitudes. At distances less than 10 kpc, the metallicity gradient is steep due to the thick disk halo transition. The MO, around 10 kpc, also appears to be a distinct feature in the mean metallicity compared to the "underlying" distribution seen again beyond ~15 kpc. Below 7 kpc, the stellar populations are most likely too complex for our simple approach as seen in the large error bars irregular profile. For a complete discussion on the metallicity of the MO, see Section 4.4.

Figure 9 shows the comparison between the two models in the Galactic latitude range from 5° to 25°, as probed by the survey. The Martin et al. (2004) model (upper panels of Figure 9) shows a slight decrease in Galactic latitude across the survey and describes a distinct stellar stream predominantly below $b = 20°$. Peñarrubia et al. (2005; lower panels of Figure 9) have a tidal stream model which is found mostly at higher latitudes. In this manner, we should expect to see a decrease in density at higher latitudes for the Martin et al. (2004) model and an increase in density for the Peñarrubia et al. (2005) model. In the middle upper and lower panels of Figure 9, it is shown that the observations roughly match both models although the measured change in density (see Table 3) is contrary to both models. In terms of the height above the plane (right panels of Figure 9) the overdensity seems to be slightly closer at higher latitudes than at lower latitudes, although with the errors it is consistent with a vertical feature. Both models seem to bracket a possible tidal stream scenario for the MO as determined through this survey. Although the structure of the stream seen in the data is not compatible with either simulation it is difficult to exclude a tidal stream solution since the large number of parameters practically ensures a suitable model is likely to be found.

4.2. The Monoceros Overdensity as the Galactic Flare

The MO is a low-latitude stellar structure and, as such, could be related to the generic structure of the disk. Although many investigations have pursued this possibility (Momany et al. 2004, 2006; Moitinho et al. 2006; López-Corredoira et al. 2007; Hammersley & López-Corredoira 2011), the distance to the MO typically precludes a definitive conclusion since the MO stars are faint and removing contaminants is highly problematic. Recently, Hammersley & López-Corredoira (2011) have attempted to show that the stellar profiles seen in the directions of the MO are compatible with the flaring of the galactic disk. The flare
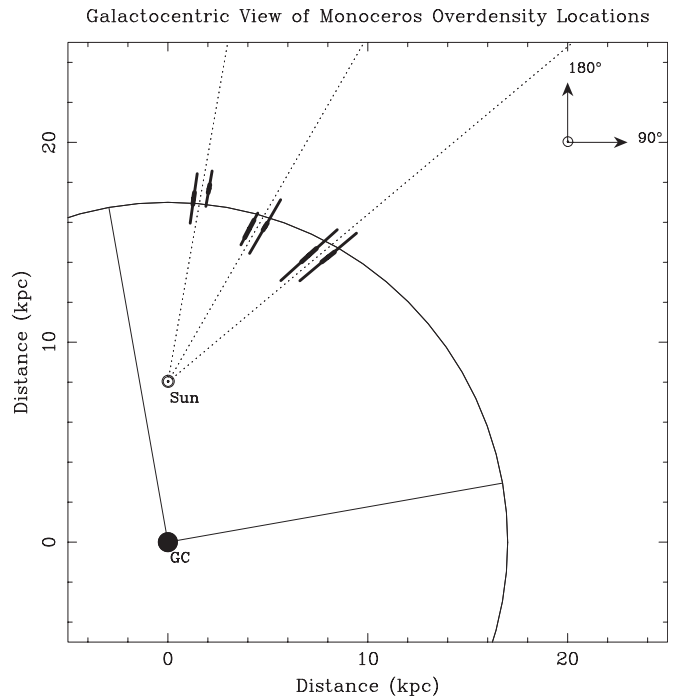

Figure 8. Galactocentric locations and distances of the MO in each of the three stripes. The thick line shows the error on the distance estimate while the thin line shows the depth of the stream. The dashed line is the direction of each of the stripes. The lower latitude fields plotted to the right of the line and the higher latitude fields to the left. The Sun is located 8 kpc from the center and the solid line is a galactocentric circle with radius 17.0 kpc. The lines from the galactic center are visual aids to highlight the circularity of the curved line.

Table 4
Flare Parameters Used in Equation (1) from
Hammersley & López-Corredoira (2011)

Parameter	Value
Thin disk scale height ($h_{z,\mathrm{thin},\odot}$)	186 pc
Thin disk scale length ($h_{R,\mathrm{thin}}$)	2400 pc
Thick disk scale height ($h_{z,\mathrm{thick},\odot}$)	631 pc
Thick disk scale length ($h_{R,\mathrm{thick}}$)	3500 pc
Solar radius ($R_\odot$)	7900 pc

is described such that beyond a certain radius, the disk rapidly thickens and becomes prominent above the plane, replicating the effect of the MO stars. They sample a small range of galactic longitudes, mostly in regions unaffected by the galactic warp, and fit a small range of flare models to the SDSS CMDs. They conclude that the stellar counts can be accounted for with the galactic flare starting at 16 kpc galactocentric and using a scale length of ~4.5 ± 1.5 kpc.

Although the CMD-fitting method presented here differs significantly from the star count approach used in Hammersley & López-Corredoira (2011), we have fitted their flare models to our data set across a large parameter space of flare scale lengths and flare onset positions to further investigate this scenario. In this regard, we also use the equations below to define the flare as described in their paper. Table 4 lists the constants used in the model. For convenience, we reproduce them here (Equation (2)). Note that R_i is the radius at which the flare starts, A is a scale factor for the density, ρ_{thin} is the density of the thin disk, ρ_{thick} is the density of the thick disk, ρ_{halo} is the density of the halo, h_{rf} is the flare scale length, R is the galactocentric radius, and z
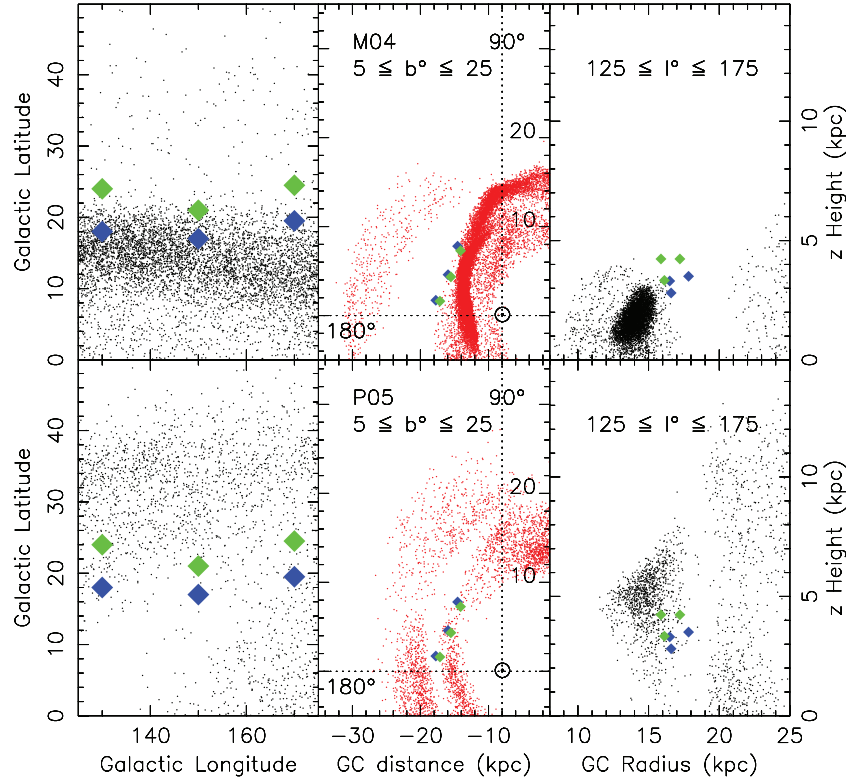
Figure 9. Left panels: Martin et al. (2004; top) and Peñarrubia et al. (2005; bottom) in the same region as surveyed in this paper. The green diamonds show the mean latitude of the upper half of this survey and the blue diamonds show the mean latitude of the lower half of this survey. Center panels show the top down galactocentric view of the models in the second quadrant. The distances to MO are shown with both green and blue filled diamonds. Right panels show the cross-section view of the tidal models with galactocentric radius on the x-axis and height above the plane on the y-axis.

(A color version of this figure is available in the online journal.)

is the height above the disk:

$$\rho_{\text{total}} = \rho_{\text{thin}} + \rho_{\text{thick}} + \rho_{\text{halo}}$$

$$\rho_{\text{thin}} = A \left[\frac{h_{z,\text{thin},\odot}}{h_{z,\text{thin}}(R)} \right] \exp\left[-\frac{R - R_\odot}{h_{R,\text{thin}}} \right] \exp\left[-\frac{|z|}{h_{z,\text{thin}(R)}} \right]$$

$$\rho_{\text{thick}} = 0.09A \left[\frac{h_{z,\text{thick},\odot}}{h_{z,\text{thick}}(R)} \right] \exp\left[-\frac{R - R_\odot}{h_{R,\text{thick}}} \right] \exp\left[-\frac{|z|}{h_{z,\text{thick}(R)}} \right]$$

$$\rho_{\text{halo}} = 1.4 \times 10^{-3} A \frac{\exp\left[10.093 \left(1 - \left(\frac{R_{sp}}{R_\odot} \right)^{1/4} \right) \right]}{(R_{sp}/R_\odot)^{7/8}}$$

$$h_{z,\text{thin/thick}}(R) = \begin{cases} h_{z,\text{thin/thick},\odot}, & R \leqslant R_i \\ h_{z,\text{thin/thick},\odot} \exp\left(\frac{R - R_i}{h_{rf}} \right), & R > R_i \end{cases}$$

$$R_{sp} = \sqrt{R^2 + 2.52z^2}. \qquad (2)$$

To test this model against our MO density profile we have varied both the onset point of the flare and its scale length. Figures 10 and 11 show the resulting χ^2 space with 1σ, 2σ, and 3σ contours for the global and individual fits to the data, respectively. The flare onset position varies from 1 to 21 kpc and the scale length has been varied from 0 to 10 kpc, both of which were iterated in 100 pc steps. Each model was compared against the data and the χ^2 value was determined for each point in the parameter space. Flare models with small-scale lengths describe sharp features in the density profile while large-scale lengths have long slowly varying density profiles. The data have been fitted both to find a global solution for the flare considering
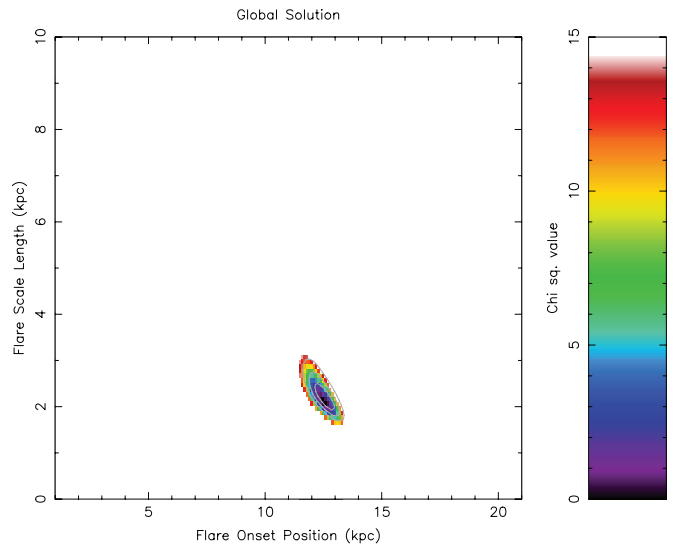

Figure 10. χ^2 space after fitting for a global solution to the galactic flare model. The onset position and scale length are free parameters in the fit with the contours showing the 1σ, 2σ, and 3σ deviations.

(A color version of this figure is available in the online journal.)

all the data and individually to highlight the differences between fields. Figure 11 shows that the MO density profile typically requires the flare model to have a very short scale length, with a global solution of 2.1 kpc and an onset radius of 12.6 kpc (see Table 5 for the best fit in each field). In Figure 12, the global model has been overplotted on each of the MO density profiles
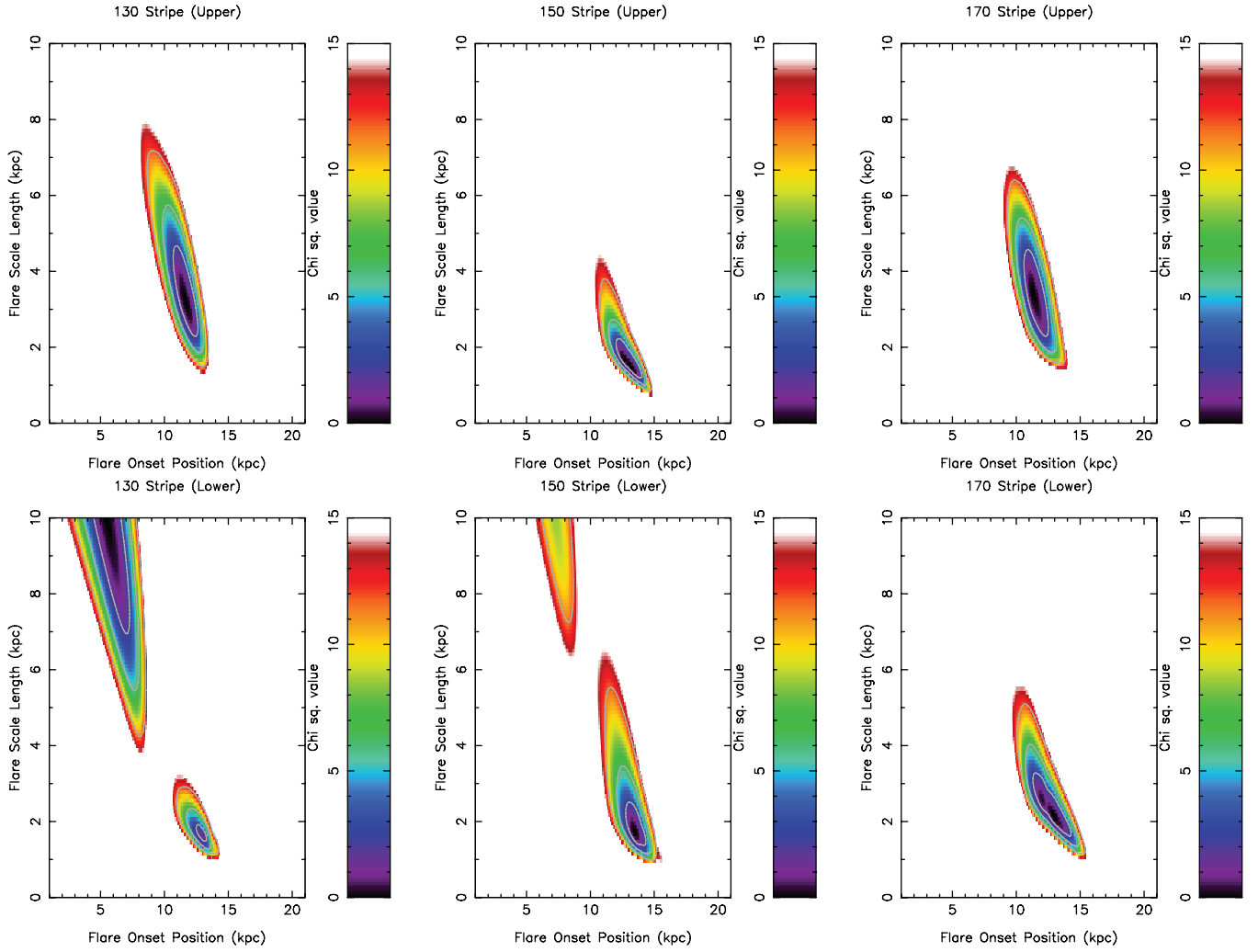
Figure 11. Each panel shows the χ^2 space after fitting a galactic flare model (Equation (2)) for the upper and lower halves of the three stripes of the survey with the global solution shown in the top-left panel. The figures show the range of onset points for the galactic flare and it is the scale length for the model tested with the resultant χ^2 plotted in color. The contours shown in each sub-panel delineate the 1σ, 2σ, and 3σ lines. In general, the best-fit models are exclusively with very small scale lengths and the onset radii increase from $\sim$12 kpc at $l = 130°$ to $\sim$14 kpc at $l = 170°$ in line with the 2 kpc change in distance seen in CMD-fitting analysis. The small-scale length, in particular, reveals the nature of the MO to be one of a short transient feature and not an extended, generic component of the disk. The minima at onset values less than 10 kpc and large-scale lengths seen in the lower halves of the $l = 130°$ and $150°$ stripes are due to the model not having a prescription for the warp and the densities mismatching at small heliocentric distances.

(A color version of this figure is available in the online journal.)

Table 5
Best Flare Model Parameters Determined by the Minima of χ^2 Map as Seen in Figure 11 with the Uncertainties Determined by the 1σ Contour Line

Field	Onset Position (kpc)	Scale Height (kpc)
Global	$12.6^{+0.3}_{-0.6}$	$2.1^{+0.3}_{-0.2}$
130 (upper)	$11.7^{+0.8}_{-1.1}$	$3.2^{+1.4}_{-1.0}$
130 (lower)[a]	12.8	1.7
150 (upper)	$13.2^{+0.7}_{-1.3}$	$1.5^{+0.7}_{-0.4}$
150 (lower)	$13.5^{+0.7}_{-0.8}$	$1.8^{+0.6}_{-0.5}$
170 (upper)	$11.3^{+1.1}_{-0.8}$	$3.5^{+1.0}_{-1.3}$
170 (lower)	$13.0^{+1.2}_{-1.8}$	$2.2^{+1.0}_{-0.7}$

Notes. [a] The lower field in the 130 stripe has no error estimate since the minima used here is not the absolute minima found in Figure 11.

for comparison with the non-flare model shown as a solid-blue line. The model of the flare used here is very basic and thus does not include a prescription for known Galactic features such as

the warp. This is clearly evident in the fields closer to $l = 90°$ where the warp becomes stronger. The mismatch at small heliocentric distances for the lower half of $l = 130°$ stripe is an example of this.

In general, this basic flare model can be fit to the data within the uncertainties for the majority of the points. While the presence of the warp is clearly responsible for the discrepancies at small heliocentric distances, it is unclear whether the differences between the MO density profile and the generic properties of the flare model should be explained by the noise in the data or an intrinsic irregularity of the outer disk. The flare parameters found here are consistent with that found by Mateu et al. (2011; onset $\sim$11.5 kpc, scale length $\sim$1.6 kpc), using RR Lyrae stars to trace the outer thick disk. However, this is a much shorter scale length and onset radius than that found by Hammersley & López-Corredoira (2011; onset $\sim$16 kpc, scale length $\sim$4.5 ± 1.5 kpc). This difference potentially arises from the fact that Hammersley & López-Corredoira (2011) push to stars with increasing photometric errors which will inherently
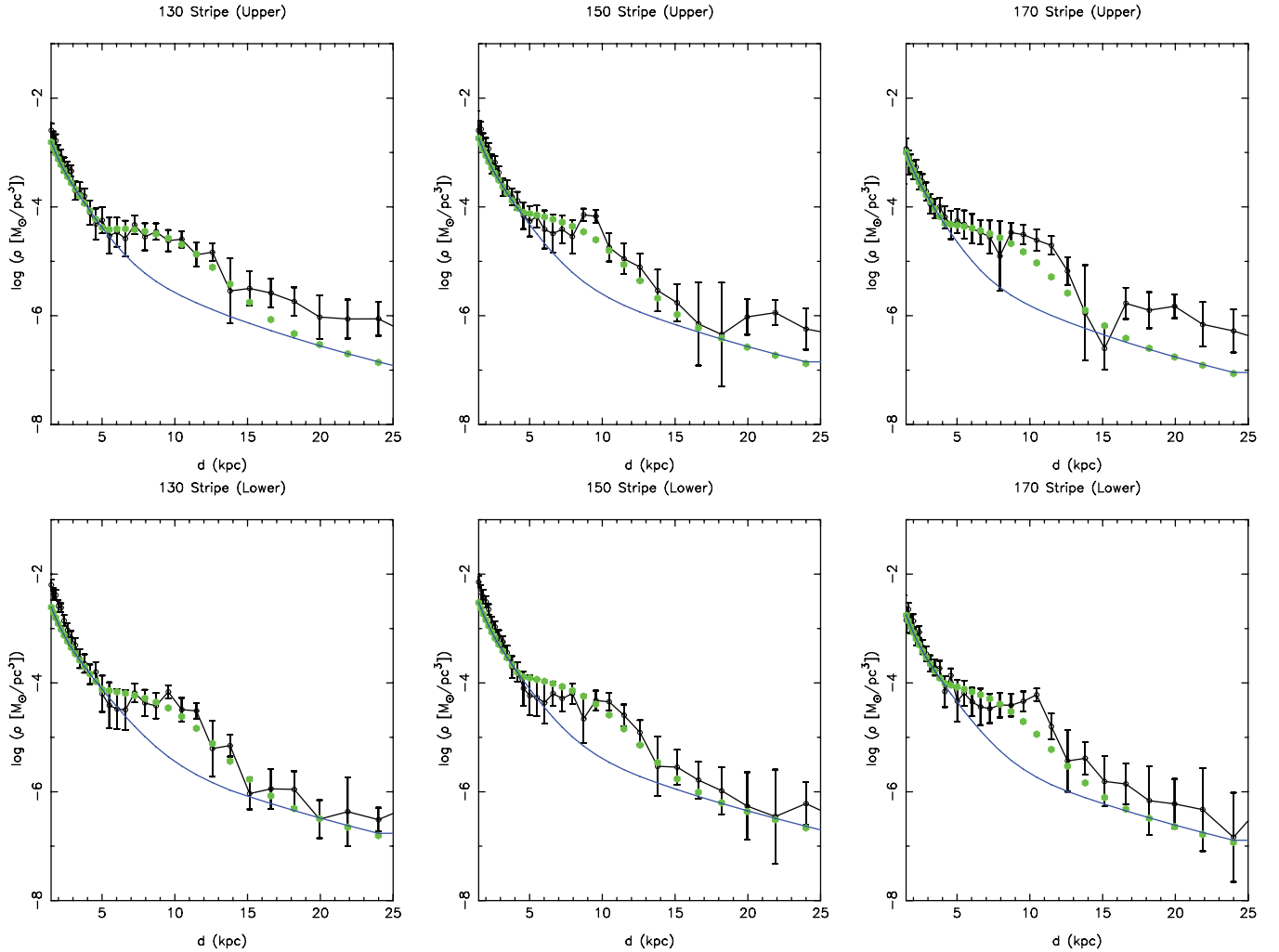
Figure 12. CMD-fitting analysis density profiles for each of the upper and lower halves of the three stripes of the survey overplotted with the global galactic flare model (green points) plotted against heliocentric distance. The non-flare model is shown as a solid-blue line. A discrepancy within the first 5 kpc is due to the presence of the warp which is unaccounted for by this model and the $l = 130°$ lower half-stripe has a minima due to this mismatch. Overall, the global flare model is within the error bars although in several fields it does not trace the peak and is consistently lower than the data at large galactic radii.

(A color version of this figure is available in the online journal.)

smear out their result. Figure 11 shows that a scale length of $\sim 4.5 \pm 1.5$ kpc is feasible at the 2σ–3σ level but a flare onset position of 16 kpc is not likely with our data. Improved number statistics might be necessary to reduce the uncertainties in the MO density profile and thus we could determine whether the deviations from the smooth model can be considered significant or simply the nature of the outer disk itself.

4.3. The Monoceros Overdensity as a Perturbed Disk

There is the possibility that the MO could be explained through a disrupted disk scenario whereby the disk interacts with a massive dark matter sub-halo. In this scenario, no new stars are added to the disk but rather the existing disk stars are swept or migrated into large spiral or ring-like structures. Models illustrating this scenario can be found in Kazantzidis et al. (2008), Younger et al. (2008), Purcell et al. (2011), and Gómez et al. (2012). All the authors find that the structures are typically ~ 4 Gyr old and so are relatively long lived.

Distinguishing between these and a tidal stream is difficult and most likely requires detailed velocities or chemical abundance information. Fortunately, some insights into whether this scenario is feasible can be seen in the stellar density profiles

as shown in Purcell et al. (2011). In their model, the resulting stellar density profile with heliocentric radius has significant substructure. Since the overdensity is not created with new stars but rather a rearrangement of the disk, it follows that creating an overdensity naturally produces a corresponding underdensity. In this manner, both their light and heavy Sagittarius-like dwarf galaxy encounters induce significant underdensities in the disk, adjacent to the ring-like overdensity of around 1.2 dex (see Figure 4(b) and S7 from Purcell et al. 2011). Crucially, there is no evidence for these underdensities in our data set that could possibly match the dramatic change in the stellar density profile as suggested by their model. Additionally, to place stars at the location of the MO detections ~ 5 kpc above the plane is limited to their simulation with a heavy Sagittarius dwarf galaxy. The light version is unable to have such an impact on the scale heights of the disk stars.

4.4. The Metallicity of the Monoceros Overdensity and the Outer Disk

The metallicity of the MO has been measured both photometrically and spectroscopically with a variety of results. Photometrically, the metallicity has been found to be [Fe/H] $\sim$

-0.95 ± 0.15 from Ivezić et al. (2008), [Fe/H] ~ -1.0 from Sesar et al. (2011), and [Fe/H] ~ -1.0 from this study. Spectroscopically, it has been reported as [Fe/H] $\sim -1.6 \pm 0.3$ by Yanny et al. (2003), [Fe/H] $\sim -0.4 \pm 0.3$ by Crane et al. (2003), $< $[Fe/H]$ > \sim -1.37 \pm 0.04$ by Wilhelm et al. (2005), $-1.04 \leqslant$ [Fe/H] $\leqslant -0.1$ by Chou et al. (2010), and most recently by Meisner et al. (2012) with [Fe/H] $= -1.0$. From this, it is clear that the MO is a complex stellar population that is consistently metal-poor.

Characterizing the disk at the distances of the MO is difficult and so the expected metallicity profile needs to be extrapolated from our understanding at smaller galactocentric radii. To do this, we utilize five studies of the outer disk (Coşkunoğlu et al. 2012; Lee et al. 2011; Cheng et al. 2012; Ivezić et al. 2008; Yong et al. 2005) to understand how the disk evolves at these distances. Using the SEGUE survey, Lee et al. (2011) traced the metallicity of the thin and thick disks beyond 2 kpc from the Sun showing that the mean [Fe/H] of the thin disk is ~ -0.2 and for the thick disk ~ -0.6. Cheng et al. (2012) also find similar results with SEGUE finding that stars between 1.0 and 1.5 kpc above the plane have a metallicity of $-0.3 \leqslant$ [Fe/H] $\leqslant -1.0$, centered on [Fe/H] ~ -0.6. In terms of metallicity gradients, Coşkunoğlu et al. (2012) have shown with the RAVE[10] dwarf stars that while the thin disk decreases in metallicity by -0.043 dex/kpc^{-1}, the thick disk is essentially flat. Both Lee et al. (2011) and Cheng et al. (2012) also find the thick disk to have no metallicity gradient. Yong et al. (2005) explored the outer disk in the third galactic quadrant using open clusters and also found a flat distribution with [Fe/H] ~ -0.6. Bensby et al. (2011) confirm the metallicity gradient in the thin disk as their target stars in the galactocentric distance range of 9–13 kpc have thin disk abundance patterns with a mean metallicity of [Fe/H] $\sim -0.48 \pm 0.12$, which is significantly more metal-poor than the local thin disk stars. Extrapolating the metallicity gradient of -0.066 dex/kpc^{-1} from Cheng et al. (2012) to the radii of the MO, we find a predicted thin disk metallicity of [Fe/H] ~ -0.44, which is still more metal-rich than all estimates of the MO metallicity.

A final possibility remains that the metallicity derived through isochrone fitting is wrong, simply because we have utilized old metal-poor isochrones which would be unsuitable for a thin disk population. If the MO were thin disk stars then a 4 Gyr isochrone would better represent such a population. In this case, the isochrone would be bluer by $(g_o - r_o) \sim 0.1$ and so could feasibly be consistent with our data. The difficulty with this approach is that a 4 Gyr old MSTO star is at least 1 mag brighter than the corresponding 10 Gyr star. At the turnoff magnitudes seen in the data, $g_o \sim 19$, this translates into an additional 5 kpc in line-of-sight distance, placing the MO at ~ 21.5 kpc Galactocentric. Naively extrapolating the metallicity of the disk to these distances results in [Fe/H] ~ -0.7. The MO though is now 10 kpc above the plane and so at each turn it becomes harder to associate thin disk stars with the MO. If the thick disk truly exhibits no change in its metallicity distribution with radius then the MO also remains more metal-poor than the thick disk at these large radii.

Given this understanding of the outer disk, we can interpret the likelihood of the different formation scenarios with the metallicity finding of this study. It is important to note that this method of determining the metallicity relies on the bulk properties of the stars in the CMD and is not a direct measure of distinct components like the thick disk and halo. Rather, the profile as seen in Figure 7 shows how the contributions of the halo stars become more dominant with increasing distance and so the average metallicity of the stellar populations present is increasingly more metal-poor with heliocentric distance. The MO is therefore a distinct population which abruptly appears against this smooth transition to a pure halo population beyond the disk.

Tidal stream scenario. Distinguishing between local disk stars and stream stars from a merger is perhaps clearest in the chemical abundance patterns as shown in the review by Tolstoy et al. (2009). There are distinct chemical differences between local MW stars and stars from nearby galaxies that reveal their different enrichment histories. Recent studies of the MO using spectroscopically determined abundances (e.g., Chou et al. 2010; Meisner et al. 2012) show that the chemical properties of the MO are closer to a Large Magellanic Cloud or Sagittarius Dwarf galaxy type abundance pattern than a pure Milky Way disk population. This offset in metallicity between the MO and outer disk suggests potentially a different origin for these stars. Peñarrubia et al. (2006) suggest that the outer disk could have been created through a series of mergers in which case the abundance pattern and the consistently metal-poor nature of the MO member stars are supportive of this scenario. Additionally, Carollo et al. (2010) discuss the similarities between the metal-weak thick disk (MWTD) and the MO suggesting the two may be related. Indeed the MWTD itself is presented in Carollo et al. (2010) as distinct to the canonical thick disk and as such is possibly the result of a merger with the Milky Way disk. Together the evidence builds that the MO is an accretion event although there is no viable progenitor and its passage through the outer disk is still unknown.

Galactic flare scenario. Although the flare model of Hammersley & López-Corredoira (2011) does not make any predictions about the metallicity of the stars, our understanding of the disk can be used to determine whether the MO metallicity is consistent with a Milky Way population. It is clear from Figure 7 that the stars along our lines of sight have a steadily declining metallicity with distance and the stars bracketing the MO typically have abundances of $-1.2 <$ [Fe/H] < -1.5. Thus the MO appears distinct in the outer disk as more metal-rich than the nearby stars. A comparison between these metallicities and those described in Ivezić et al. (2008) suggests that at these distances we are beginning to probe the inner halo prior to MO and beyond the MO there is a clean halo sample. Clearly, these stars are apart from the main disk population but it is difficult to explain why the MO is so metal-poor if it is simply an extension of the underlying disk. The flare is undoubtedly a real phenomenon but to what extent and what influence it has in the outer disk is uncertain.

Perturbed disk scenario. The stars which are perturbed into the MO-like structure seen in Purcell et al. (2011) are sourced from across the entire disk. The member stars are migrated from inside and outside of the final location and so the resultant metallicity should be an average of these contributing locations in the disk. Since the disk, in general, is more metal-rich than the MO and there are very few locations within the disk that could supply stars more metal-poor than the MO, it is highly unlikely that an aggregate population as proposed by this model could achieve the metal-poor status of current set of MO metallicity estimates. Since our findings too confirm the metal-poor nature of the MO, the perturbed disk scenario with

---

[10] RAdial Velocity Experiment.

Table 6
Column Information and Format

Column Number	Label	Type	Column Number	Label	Type
1	Right ascension (hours)	Integer	11	Y pixel g	Real
2	Right ascension (minutes)	Integer	12	g mag	Real
3	Right ascension (seconds)	Real	13	g mag error	Real
4	Declination (degrees)	Integer	14	g classification	Integer
5	Declination (minutes)	Integer	15	X pixel r	Real
6	Declination (seconds)	Real	16	Y pixel r	Real
7	Galactic longitude (l)	Real	17	r mag	Real
8	Galactic latitude (b)	Real	18	r mag error	Real
9	Chip	Integer	19	r classification	Integer
10	X pixel (g)	Real	20	$E(B-V)$	Real

its predicted observable properties, as described by Purcell et al. (2011), is not feasible given the data.

5. CONCLUSION

We have presented new distance, density, and metallicity measurements for the stellar MO in the outer Milky Way, based on SUPRIME-CAM wide field imaging data and a CMD-fitting analysis. Our distance measures are the most quantitative estimates to date for the MO.

The MO appears as a wall of stellar material at roughly 10 kpc from the Sun at the galactic longitudes of 130°, 150°, and 170°, and galactic latitudes of +15° ⩽ b ⩽ +25°. Detections of the MO have been confirmed between 3 and 5 kpc above the plane and consist of a metal-poor population with an average metallicity of [Fe/H] ~ −1.0.

We consider these findings in the light of the three formation scenarios currently in the literature: (1) a tidal stream origin, (2) the galactic flare, and (3) the perturbed disk. We find that:

1. Tidal stream models from the literature bracket the distances and densities we derive for the MO. Furthermore, recent results for the chemistry of stars in the MO support an extragalactic origin. This suggests that a tidal stream model can be found that would fully fit the MO data. On the other hand, the large parameter space available for this model, the orbit, mass, inclination, and eccentricity of the merger, amongst others, presents the danger that such a fit—while possible—might not be the true explanation for the MO.

2. The flaring of the galactic disk provides another possibility for explaining the presence of these stars at large distances from the plane. We fitted a large range of galactic flare models finding a solution with a mean onset radius of 12.6 kpc and a scale length of 2.1 kpc that is a reasonable match to the data. This is similar to the findings of Mateu et al. (2011) but is much smaller than the models suggested by Hammersley & López-Corredoira (2011). The main difficulties with the flare model are (1) whether the basic flare model used here while consistent with the data would be applicable across wider latitude and longitude ranges and (2) the metallicity ([Fe/H]) derived in this paper as well as the determinations from other sources (see Section 4.4) is building a consistent picture that the disk is too metal-rich to source the MO stars. If the disk can be shown to be metal-poor at these radii then the flare scenario is indeed a possibility.

3. The perturbed disk scenario makes clear testable predictions about the metallicity and stellar density profile of a MO-like feature. Both of these are incompatible with the

data: the MO stellar density profile does not contain the significant underdensities predicted by the model while the metallicity of the MO is too metal-poor even for a population of stars sourced from across the disk.

It is clear that the MO still lacks the observational evidence required to unequivocally determine its origins. However, the deep observations we have presented here, coupled with CMD-fitting techniques, are able to constrain its properties to much greater precision than has previously been possible. We have ruled out the "perturbed disk scenario" for the MO, and found key problems that must be solved if the MO is to be explained by a flared disk. Given the distance to the MO and the uncertainty over its origin, it is crucial to minimize the photometric errors so as to limit their impact when deriving its properties. Further studies of the MO should include high-precision photometry to better constrain the physical dimensions of the MO coupled with high-resolution spectroscopy for a detailed abundance analysis. This combined approach seems best suited to unraveling the origin of the MO feature.

APPENDIX

ONLINE DATA

The data presented in this paper are being made available online and all issues related to the data can be addressed to conn@mpia-hd.mpg.de. The data consist of all objects extracted from each reduced frame in the survey, galaxies, and stars, although poor data have been excised from the final catalog. Individual reduced frames will be available upon request. The catalog mostly follows the layout of the Cambridge Astronomical Survey Unit Wide Field Camera Pipeline (Irwin

Table 7
Example Data from the Catalog

Column 1	Column 2	Column 3	Column 4	Column 5	Column 6	Column 7	Column 8	Column 9	Column 10
5	32	29.55	62	16	34.7	149.930191	15.2970066	1	1553.4
5	32	40.61	62	14	34.4	149.971298	15.2990808	1	1162.8
5	32	30.45	62	7	57.5	150.060394	15.2272711	1	1517.3
5	32	30.43	62	12	27.5	149.992889	15.2644424	1	1522.6
5	32	42.7	62	16	15.0	149.948212	15.3164396	1	1087.9
5	33	7.83	62	6	31.6	150.119278	15.2787237	1	184.5
5	32	35.22	62	5	13.7	150.106125	15.2127686	1	1343.1
5	32	58.89	62	14	42.0	149.987595	15.3309498	1	512.7
5	33	6.82	62	6	24.8	150.119965	15.2760792	1	220.4
5	32	41.21	62	15	37.5	149.956116	15.3087721	1	1141.0

Col 11.	Col 12.	Col 13.	Col 14.	Col 15.	Col 16.	Col 17.	Col 18.	Col 19.	Col 20.
3848.9	22.552	0.018	−1	1550.4	3851.3	21.162	0.011	−1	0.113
3248.3	22.56	0.019	−1	1159.7	3250.6	21.157	0.011	−1	0.145
1251.9	22.555	0.019	1	1514.4	1254.1	20.76	0.0080	1	0.126
2602.9	22.527	0.019	1	1519.6	2605.2	21.508	0.015	1	0.102
3758.9	23.611	0.019	0	1084.8	3761.4	3.616	0.0	0	0.198
840.7	22.586	0.019	1	181.2	842.9	20.898	0.0090	1	0.122
436.8	22.496	0.019	−1	1340.2	438.9	22.293	0.03	−1	0.114
3300.5	22.61	0.019	−3	509.4	3302.9	21.231	0.011	1	0.109
806.1	22.596	0.019	−1	217.2	808.2	21.087	0.01	−1	0.108
3567.9	22.613	0.019	−1	1138.0	3570.4	21.07	0.01	−1	0.109

Table 8
Field Centers for the Individual Pointings of the Survey

Field Name	Galactic Longitude (l)	Galactic Latitude (b)	R.A. (deg)	Decl. (deg)	Airmass (g)	Airmass (r)
130_01	129.505203	15.2144403	41.34738719353522	76.60936674102940	1.83	1.88
130_02	129.498260	15.5623217	41.99728376377872	76.92390791959453	1.85	1.89
130_03	129.520309	15.9293108	42.83053801772657	77.24082916240711	1.87	1.91
130_04	129.490295	16.3293571	43.57344637209229	77.60785831085641	1.88	1.93
130_05	129.477982	16.7765141	44.54271403857756	78.00559018571801	1.90	1.95
130_06	129.488922	17.2290936	45.68634624732895	78.39321646040258	1.93	1.98
130_07	129.481201	17.7492542	47.01153201618068	78.84294581324289	1.95	2.00
130_08	129.486389	18.2244434	48.36961137572538	79.24196293987690	1.98	2.03
130_10	129.891327	18.6489811	51.37118049084526	79.37541996407468	1.99	2.05
130_11	130.495422	18.4339542	53.12960548181101	78.86147318029894	1.96	2.03
130_12	129.932236	19.6258717	54.88780147544033	80.12706264257046	2.04	2.10
130_13	130.272293	19.6864243	56.53253062677564	79.96761144072845	2.03	2.10
130_14	130.025726	20.5192966	58.82546202768954	80.74218057326074	2.08	2.16
130_15	130.352402	20.5899010	60.48630003355603	80.58115326477444	2.08	2.15
130_16	129.884949	21.1346321	60.96542286637656	81.27529378945327	2.12	2.20
130_20	129.500458	23.1141567	70.27297710747496	82.82702811918269	2.20	2.21
130_21	129.786774	23.3386803	72.92685925574828	82.73512051347623	2.19	2.21
130_22	129.711731	23.7662678	75.57591317062941	83.01743603239895	2.21	2.23
130_23	129.709274	24.1529255	78.39220828275825	83.20574701910283	2.23	2.26
130_24	130.074417	24.3651276	81.19850907262055	83.00000442870187	2.21	2.25
130_25	130.503357	24.6074963	84.23756455977386	82.73757597853790	2.20	2.24
130_26	129.883682	25.2132816	87.35185357260404	83.47482960191130	2.26	2.30
130_27	130.162216	25.6129627	91.31864264785848	83.34836976965003	2.25	2.31
130_28	130.274887	25.7499065	92.67235820452719	83.28326763729932	2.25	2.31
130_29	129.845047	26.3427334	97.17409024268696	83.77700149427237	2.30	2.37
150_01	149.367172	14.7309074	81.47717324443296	62.45923524113733	1.54	1.75
150_02	150.021484	15.0184927	82.70019456402970	62.06101665160047	1.53	1.44
150_03	150.568130	15.1846695	83.56255315448394	61.68566109101802	1.53	1.43
150_04	149.267120	15.8481741	83.48413227595164	63.10354272409283	1.55	1.46
150_05	149.467026	16.1752510	84.32222788603623	63.09321359738084	1.55	1.46
150_06	149.739899	16.3192616	84.87544284777340	62.93090358029885	1.54	1.46
150_07	149.869659	16.5827961	85.51538476758475	62.94394993994977	1.54	1.46
150_08	150.418961	16.8561764	86.57224144450691	62.60087744573428	1.53	1.45
150_09	149.855774	17.7393131	87.79741617372791	63.47297203588319	1.55	1.47
150_10	149.978928	17.9487495	88.33340417316249	63.45655395917793	1.55	1.47
150_11	149.595703	18.8632870	89.88188730710624	64.16482959621780	1.58	1.50

Table 8
(Continued)

Field Name	Galactic Longitude (l)	Galactic Latitude (b)	R.A. (deg)	Decl. (deg)	Airmass (g)	Airmass (r)
150_12	149.404037	18.9116516	89.81690579089114	64.35037968901068	1.57	1.50
150_13	149.469101	19.4710522	91.06547830802131	64.51266042943159	1.58	1.50
150_14	149.498032	19.8628922	91.93500344111298	64.63475959071147	1.58	1.51
150_15	149.465454	20.0847473	92.39163688508779	64.74451585942646	1.58	1.51
150_16	149.472748	20.4829426	93.27157679386292	64.88004096575455	1.59	1.52
150_17	150.229660	20.8936558	94.73593492322217	64.35456695208589	1.58	1.51
150_18	149.338928	21.2984161	94.99382608269545	65.27239075985462	1.60	1.53
150_19	150.334595	21.2837868	95.66243700857011	64.38920170930041	1.58	1.51
150_20	150.471024	21.6856174	96.63736873754850	64.39421276382994	1.58	1.51
150_21	149.105026	22.5320530	97.67760865552893	65.85253465676418	1.62	1.55
150_22	150.136307	22.7098103	98.72154312222851	64.98692367067588	1.60	1.53
170_05	170.197723	16.5303841	99.33109348057584	45.13093652864079	1.11	1.16
170_06	170.188751	17.0044270	99.95114873787325	45.31547803482419	1.11	1.16
170_07	169.485580	17.7562637	100.6056548374478	46.21387973809730	1.12	1.17
170_08	169.477707	18.0655041	101.0199755684189	46.33078105947673	1.12	1.17
170_09	169.961853	18.3975201	101.7015952165405	46.01629271848925	1.12	1.17
170_10	170.181961	18.6210308	102.1070410738897	45.89765781774504	1.11	1.17
170_11	169.297699	19.4511223	102.8321404576463	46.96444993027531	1.12	1.18
170_12	169.478622	19.8252201	103.4316191531833	46.92585236294776	1.12	1.18
170_13	169.431854	20.2172241	103.9554434974554	47.09324064970371	1.13	1.18
170_14	169.017380	20.3716507	103.9902628410851	47.51086788331664	1.13	1.18
170_15	169.785507	20.5863171	104.6219604394106	46.89467570845383	1.12	1.18
170_16	170.062866	21.1207714	105.4821103329919	46.81214457363338	1.12	1.18
170_17	169.436630	21.6631756	105.9884280355083	47.53028736542868	1.13	1.18
170_18	170.377396	21.3885803	105.9831545077192	46.61307929154813	1.12	1.17
170_19	170.731049	22.1850262	107.2307431939022	46.53162776193600	1.12	1.17
170_20	169.043121	22.7703648	107.4179425403126	48.19269113131208	1.14	1.19
170_21	169.394073	22.6403027	107.3635388673966	47.84569174336261	1.14	1.18
170_22	170.449234	22.9586735	108.2095068314083	46.99719888558490	1.13	1.17
170_23	170.113739	24.0381660	109.6265273415698	47.57695394709530	1.13	1.18
170_24	170.010727	24.2990913	109.9668119381534	47.73308269329995	1.14	1.18
170_25	169.622864	24.6615162	110.3634621605747	48.16363440273511	1.14	1.19
170_26	169.925446	25.1457653	111.1647343607107	48.01089193383915	1.14	1.19
170_27	170.744507	25.3222599	111.6741012150978	47.33086267226461	1.13	1.18
170_28	170.499222	25.7041969	112.1500983351095	47.63318062885149	1.14	1.18
170_29	169.509598	26.5984821	113.1763707919120	48.69161945583298	1.15	1.20
170_30	169.204178	27.2056103	114.0004198180252	49.07784152319226	1.15	1.20
170_31	169.042969	27.5770073	114.5180484244156	49.28747251547379	1.15	1.20
170_32	170.136215	27.5013657	114.6775481523616	48.32084412581273	1.14	1.19

Note. g- and r-band observations have the same pointing centers.

& Lewis 2001) with the addition of the Galactic coordinates for each object, right ascension and declination are in J2000.0. Due to the large size of the full catalog, we have split the data set into three portions based on the primary field designation. The data for fields 130 (37.7MB), 150 (53.5MB), and 170 (66.8MB) are available in the online version in FITS format.

The descriptors for each column in the catalog are shown in Table 6 and an example of the data is shown in Table 7. The classification scheme is as follows: Stellar are -1, Possible Stellar are -2, non-Stellar/Galaxy are 1, Noise is 0, Possible non-Stellar/Galaxy is -3, Cross-match problem is -8, and Saturated object is -9. The entire catalog contains 3.4 millions objects and the breakdown per filter in the entire catalog is $\sim$643,000 Stellar, $\sim$550,000 Possible Stellar, $\sim$747,000 non-Stellar/Galaxy, and $\sim$411,000 Possible non-Stellar/Galaxy in the g band. The r band has $\sim$625,000 Stellar, $\sim$432,000 Possible Stellar, $\sim$764,000 non-Stellar/Galaxy, and $\sim$320,000 Possible non-Stellar/Galaxy.

The data here have been extinction corrected following the standard prescription when the extinction is less than $E(B-V) \leqslant 0.1$, otherwise the relation from Bonifacio et al.

(2000), as shown in Equation (A1), has been used. The dust values have been extracted from the Schlegel et al. (1998) maps using the dust_getval.c program:

$$\text{dust value} = 0.1 + 0.65(E(B-V) - 0.1). \quad (A1)$$

The data have also been corrected for airmass. The airmasses and field centers for each field can be found in Table 8. Individual objects do not have an identifier that relate them to a particular field; however, most objects will be easily matched with its corresponding field center. Objects in overlap regions can be associated with a particular field based on the chip in which they reside. In this regard, users should note that duplicate observations of the same object have not been removed from the catalog. They have been left in to allow the user to gauge the relative depths of each pointing.

REFERENCES

Adelman-McCarthy, J. K., Agüeros, M. A., Allam, S. S., et al. 2008, ApJS, 175, 297
Belokurov, V., Zucker, D. B., Evans, N. W., et al. 2006, ApJ, 642, L137

Bensby, T., Alves-Brito, A., Oey, M. S., Yong, D., & Meléndez, J. 2011, ApJ, 735, L46
Bonifacio, P., Monai, S., & Beers, T. C. 2000, AJ, 120, 2065
Carollo, D., Beers, T. C., Chiba, M., et al. 2010, ApJ, 712, 692
Casetti-Dinescu, D. I., Carlin, J. L., Girard, T. M., et al. 2008, AJ, 135, 2013
Cheng, J. Y., Rockosi, C. M., Morrison, H. L., et al. 2012, ApJ, 746, 149
Chou, M.-Y., Majewski, S. R., Cunha, K., et al. 2010, ApJ, 720, L5
Conn, B. C., Lane, R. R., Lewis, G. F., et al. 2007, MNRAS, 376, 939
Conn, B. C., Lane, R. R., Lewis, G. F., et al. 2008, MNRAS, 390, 1388
Conn, B. C., Lewis, G. F., Irwin, M. J., et al. 2005a, MNRAS, 362, 475
Conn, B. C., Martin, N. F., Lewis, G. F., et al. 2005b, MNRAS, 364, L13
Coşkunoğlu, B., Ak, S., Bilir, S., et al. 2012, MNRAS, 419, 2844
Crane, J. D., Majewski, S. R., Rocha-Pinto, H. J., et al. 2003, ApJ, 594, L119
de Jong, J. T. A., Yanny, B., Rix, H.-W., et al. 2010, ApJ, 714, 663
Dolphin, A. E. 2002, MNRAS, 332, 91
Freeman, K., & Bland-Hawthorn, J. 2002, ARA&A, 40, 487
Girardi, L., Grebel, E. K., Odenkirchen, M., & Chiosi, C. 2004, A&A, 422, 205
Gómez, F. A., Minchev, I., Villalobos, Á., O'Shea, B. W., & Williams, M. E. K. 2012, MNRAS, 419, 2163
Grillmair, C. J. 2006, ApJ, 651, L29
Grillmair, C. J. 2009, ApJ, 693, 1118
Hammersley, P. L., & López-Corredoira, M. 2011, A&A, 527, A6
Ibata, R. A., Irwin, M. J., Lewis, G. F., Ferguson, A. M. N., & Tanvir, N. 2003, MNRAS, 340, L21
Irwin, M. J. 1985, MNRAS, 214, 575
Irwin, M. J. 1997, Instrumentation for Large Telescopes, ed. J. M. Rodriguez Espinosa, A. Herrero, & Francisco Sánchez (Cambridge: Univ. of Cambridge Press), 35
Irwin, M., & Lewis, J. 2001, New Astron. Rev., 45, 105
Ivezić, Ž., Sesar, B., Jurić, M., et al. 2008, ApJ, 684, 287
Kazantzidis, S., Bullock, J. S., Zentner, A. R., Kravtsov, A. V., & Moustakas, L. A. 2008, ApJ, 688, 254
Lee, Y. S., Beers, T. C., An, D., et al. 2011, ApJ, 738, 187
López-Corredoira, M., Cabrera-Lavers, A., Garzón, F., & Hammersley, P. L. 2002, A&A, 394, 883
López-Corredoira, M., Momany, Y., Zaggia, S., & Cabrera-Lavers, A. 2007, A&A, 472, L47
Martin, N. F., Ibata, R. A., Bellazzini, M., et al. 2004, MNRAS, 348, 12
Martin, N. F., Irwin, M. J., Ibata, R. A., et al. 2006, MNRAS, 367, L69
Mateu, C., Vivas, A. K., Downes, J. J., & Briceño, C. 2011, RMxAC, 40, 245
Meisner, A. M., Frebel, A., Juric, M., & Finkbeiner, D. P. 2012, arXiv:1205.0807
Michel-Dansac, L., Abadi, M. G., Navarro, J. F., & Steinmetz, M. 2011, MNRAS, 414, L1
Moitinho, A., Vázquez, R. A., Carraro, G., et al. 2006, MNRAS, 368, L77
Momany, Y., Zaggia, S. R., Bonifacio, P., et al. 2004, A&A, 421, L29
Momany, Y., Zaggia, S., Gilmore, G., et al. 2006, A&A, 451, 515
Newberg, H. J., Yanny, B., Rockosi, C., et al. 2002, ApJ, 569, 245
Peñarrubia, J., Martínez-Delgado, D., Rix, H. W., et al. 2005, ApJ, 626, 128
Peñarrubia, J., McConnachie, A., & Babul, A. 2006, ApJ, 650, L33
Purcell, C. W., Bullock, J. S., Tollerud, E. J., Rocha, M., & Chakrabarti, S. 2011, Nature, 477, 301
Salpeter, E. E. 1955, ApJ, 121, 161
Schlegel, D. J., Finkbeiner, D. P., & Davis, M. 1998, ApJ, 500, 525
Sesar, B., Jurić, M., & Ivezić, Ž. 2011, ApJ, 731, 4
Skrutskie, M. F., Cutri, R. M., Stiening, R., et al. 2006, AJ, 131, 1163
Sollima, A., Valls-Gabaud, D., Martinez-Delgado, D., et al. 2011, ApJ, 730, L6
Tolstoy, E., Hill, V., & Tosi, M. 2009, ARA&A, 47, 371
White, S. D. M., & Rees, M. J. 1978, MNRAS, 183, 341
Wilhelm, R., Beers, T. C., Allende Prieto, C., Newberg, H. J., & Yanny, B. 2005, in ASP Conf. Ser. 336, Cosmic Abundances as Records of Stellar Evolution and Nucleosynthesis, ed. T. G. Barnes, III & F. N. Bash (San Francisco, CA: ASP), 371
Yanny, B., Newberg, H. J., Grebel, E. K., et al. 2003, ApJ, 588, 824
Yong, D., Carney, B. W., & Teixera de Almeida, M. L. 2005, AJ, 130, 597
Younger, J. D., Besla, G., Cox, T. J., et al. 2008, ApJ, 676, L21
Yusifov, I. 2004, in The Magnetized Interstellar Medium, ed. B. Uyaniker, W. Reich, & R. Wielebinski (Katlenburg-Lindau: Copernicus GmbH), 165